ORIGINAL ARTICLE

Discovery and evaluation of a novel ¹⁸F-labeled vasopressin 1a receptor PET ligand with peripheral binding specificity

Junqi Hu [a],[†], Yinlong Li [b],[†], Chenchen Dong [a], Huiyi Wei [a], Kai Liao [a], Junjie Wei [a], Chunyu Zhao [b], Ahmad Chaudhary [b], Jiahui Chen [b], Hao Xu [a], Ke Zhong [c], Steven H. Liang [b],[*], Lu Wang [a],[*], Weijian Ye [a],[*]

[a]Center of Cyclotron and PET Radiopharmaceuticals, Department of Nuclear Medicine & Key Laboratory of Basic and Translational Research on Radiopharmaceuticals, the First Affiliated Hospital of Jinan University, Guangzhou 510630, China
[b]Department of Radiology and Imaging Sciences, Emory University, Atlanta, GA 30322, USA
[c]Department of Pharmacy, Sun Yat-sen Memorial Hospital, Sun Yat-sen University, Guangzhou 510120, China

Abstract　The arginine-vasopressin (AVP) hormone plays a pivotal role in regulating various physiological processes, such as hormone secretion, cardiovascular modulation, and social behavior. Recent studies have highlighted the V1a receptor as a promising therapeutic target. In-depth insights into V1a receptor-related pathologies, attained through *in vivo* imaging and quantification in both peripheral organs and the central nervous system (CNS), could significantly advance the development of effective V1a inhibitors. To address this need, we develop a novel V1a-targeted positron emission tomography (PET) ligand, [¹⁸F]V1A-2303 ([¹⁸F]**8**), which demonstrates favorable *in vitro* binding affinity and selectivity for the V1a receptor. Specific tracer binding in peripheral tissues was also confirmed through rigorous cell uptake studies, autoradiography, biodistribution assessments. Furthermore, [¹⁸F]**8** was employed in PET imaging and arterial blood sampling studies in healthy rhesus monkeys to assess its brain permeability and specificity, whole-body distribution, and kinetic properties. Our research indicated [¹⁸F]**8** as a valuable tool for noninvasively studying V1a receptors in peripheral organs, and as a foundational element for the development of next-generation, brain-penetrant ligands specifically designed for the CNS.

*Corresponding authors.

E-mail addresses: steven.liang@emory.edu (Steven H. Liang), l_wang1009@foxmail.com, l_wang1009@jnu.edu.cn (Lu Wang), ywjky@foxmail.com (Weijian Ye).

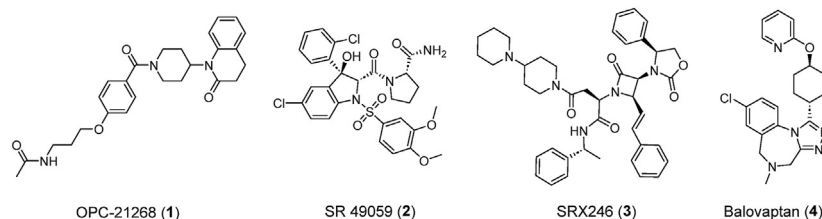†These authors made equal contributions to this work.

1. Introduction

Arginine vasopressin (AVP), a unique cyclic nonapeptide hormone, plays a vital role in various physiological functions essential for maintaining homeostasis in both the periphery and the central nervous system (CNS)[1,2]. The physiological effects of AVP are predominantly mediated by three G-protein-coupled receptors: V1a, V1b, and V2, each exhibiting distinct distribution patterns and physiological impacts. The V1a receptor, predominantly found in vascular smooth muscle, liver, adrenal gland, brain, is associated with a range of peripheral and central pathologies[3]. Studies suggest that the V1a receptor influences not only metabolic regulation, blood pressure, and vascular resistance[4-10], but also has garnered considerable attention regarding neurological conditions, social cognition and behavior[11-14]. During the 1990s, studies revealed that social and anxiety-like behaviors in rats were found to be affected by intracerebroventricular and intraseptal injections of V1a-specific antagonists[15-17], as well as by the administration of V1a antisense oligodeoxynucleotide into the septal region[18], suggesting an association between V1a receptor and these behaviors. Subsequent research has further explored the role of V1a in social cognition and behavior[19-21], and its potential implications for autism spectrum disorder (ASD)[22-26], a complex neurodevelopmental condition characterized by impaired social interaction, communication challenges, and repetitive behaviors. Despite ongoing investigations into the detailed mechanisms, the V1a receptor has emerged as a potential therapeutic target in ASD[27-32].

The multifunctional nature of V1a receptor has driven extensive research, leading to the development of numerous antagonists[33,34] (Fig. 1A). In the early 1990s, OPC-21268[35] (**1**) emerged as the first V1a-selective antago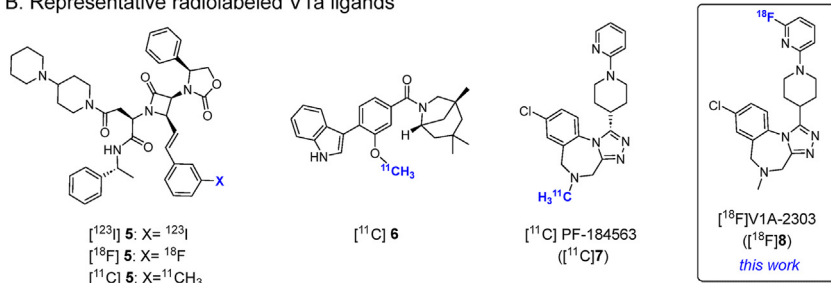nist, exhibiting high affinity for rat V1a receptor but weak affinity for human's SR 49059[36] (**2**) was noted for its high affinity, selectivity and efficacy towards both animal and human V1a receptors. In the last decade, Azevan Pharmaceuticals developed SRX246[37] (**3**), a highly selective and specific V1a receptor antagonist that proven to be safe and well-tolerated in a randomized Phase II clinical trial[38]. It can decrease anxiety-potentiated startle in healthy individuals[39], and reduce aggressive behavior in irritable Huntington's disease patients[40]. Additionally, RG7713[41] and balovaptan[42] (RG7314, **4**), discovered by Roche, have progressed into advanced clinical studies involving individuals with autism. However, despite receiving Breakthrough Therapy Designation from FDA in 2018 and showing significant efficacy on the Vineland-II scale in ASD in a Phase II trial[43], balovaptan did not demonstrate efficacy in enhancing socialization and communication in pediatric ASD patients[44] or autistic adults[45] in the subsequent Phase II or III trials. These outcomes underscore the complexity of the V1a signaling pathway and emphasize the necessity for further mechanistic studies. Hence, *in vivo* investigation of the V1a receptor system and its interaction with potential drug candidates *via* non-invasive techniques becomes imperative, offering invaluable biology insights and contributing to a comprehensive understanding of their roles and therapeutic potential.

Positron emission tomography (PET), featuring the capacity for *in vivo* imaging and quantifying biochemical processes in real-time, emerges as a promising solution for studying intricate physiological and pathological mechanisms without the need for invasive operations. The development of novel PET ligands targeting the V1a receptor remains pivotal in unraveling the complexities of physiological and pathological processes, especially in the regulation of social, emotional, cognitive behaviors. Recent

Figure 1 Representative antagonists (A) and radiolabeled ligands (B) for V1a receptor.

advancement has been made in developing radiolabeled V1a ligands (Fig. 1B), including analogs of SRX246[46] ([^{123}I]**5**, [^{18}F]**5** and [^{11}C]**5**), [^{11}C]**6**[47] and our work [^{11}C]PF-184563[48] ([^{11}C]**7**). While [^{11}C]PF-184563 stands out as the first PET ligand suitable for V1a receptor imaging in peripheral organs, there remains a need for ideal PET ligands, especially for applications both in the CNS and periphery.

This study aims to develop and validate an effective V1a-targeted PET ligand with enhanced blood−brain barrier (BBB) penetration through structural optimization. Encouraged by the results of [^{11}C]PF-184563, we hypothesized that, by maintaining binding affinity, the integration of ^{18}F into the pyridine scaffold could not only prolong the ligand half-life from 20.4 to 109.8 min but also enhance BBB permeability due to inductive effect and the shielding of the nitrogen atom on the pyridine ring. In this report, we describe the design, synthesis, pharmacological profiling, radiolabeling, and comprehensive in vitro and in vivo characterization of a novel radiolabeled analog, [^{18}F]V1A-2303 ([^{18}F]**8**), as a potential probe for PET imaging of the V1a receptor.

2. Result and discussion

2.1. Chemical synthesis

The target compound **8** was synthesized in a similar fashion based on our previous report[48]. As outlined in Scheme 1, the reaction commenced with commercially available compounds methyl piperidine-4-carboxylate **9** and 2,6-difluoropyridine **10**. Nucleophilic aromatic substitution reactions were executed to generate **11**. Subsequent steps involving hydrolysis, esterification, and hydrazinolysis, resulted in hydrazine **13** in good yield. The intermolecular cyclization of hydrazine **13** with thioamide **14** afforded 1,2,4-triazole analogue **15** in 26% yield. Boc group deprotection under acidic conditions, followed by reductive amination, led to the desired compounds **8** in 52% yield over two steps. The new compounds were fully characterized by ^{1}H and ^{13}C NMR spectroscopy and MS.

2.2. Binding affinity and BBB permeability

Having obtained target compound **8**, its biological activity and pharmacological properties were assessed through in vitro assays. As outlined in Table 1, this compound exhibited nanomolar potency and high affinity for the hV1a receptor (IC_{50} = 2.33 nmol/L and K_i = 0.46 nmol/L), which were determined using 0.03 nmol/L [^{125}I] phenylacetyl-D-Tyr(Me)-Phe-Gln-Asn-Arg-Pro-Arg-Tyr-NH_2 as radioligand, with specific binding at 85% and a B_{max} value of 2.80 pmol/mg protein. Furthermore, its binding affinities for other vasopressin receptors (V1b and V2) exceeded 10 μmol/L, highlighting excellent target selectivity.

To predict BBB permeability, the lipophilicity of compound **8** was evaluated using the shake-flask method, yielding a $logD_{7.4}$ of 1.81 ± 0.01 (n = 3). This suggests that it may be suitable as a ligand for PET imaging in the brain since molecules typically pass through the BBB via passive diffusion when $logP$ or $logD$ values fall between 1 and 3.5[49]. MDCK-MDR1 experiments showed an apparent permeability coefficient $P_{app[A−B]}$ of 33.48 × 10^{-6} cm/s (values > 10 × 10^{-6} cm/s suggesting high BBB permeability),

Table 1 Pharmacological and physiochemical properties of target compound **8**.

Pharmacology properties	Value	Physiochemical properties	Value
hV1A IC_{50} (nmol/L)	2.33	Mw (g/mol)	412.9
hV1A K_i (nmol/L)	0.46	$LogD$ (pH 7.4)	1.81 ± 0.01
hV1B IC_{50} (nmol/L)	>10,000	$P_{app\ [A−B]}$ (× 10^{-6} cm/s)	33.48
hV2 IC_{50} (nmol/L)	>10,000	Efflux ratio	0.85
		LogBB	−0.09
		MPO score	5.3
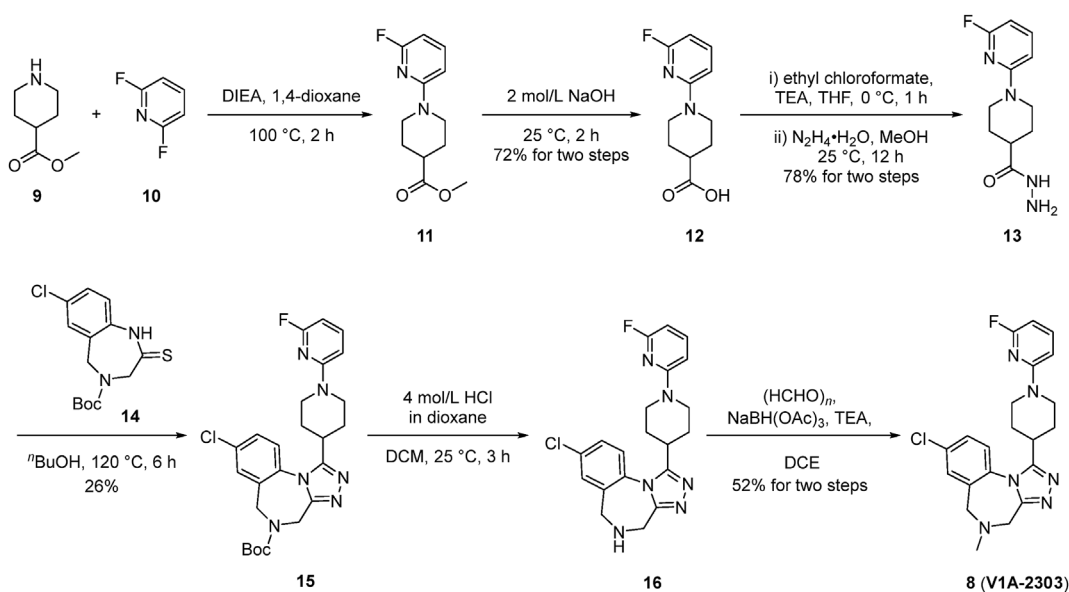
Scheme 1 Synthesis of target compound **8**.

and an MDR1 efflux ratio (ER) of 0.85, suggesting that the compound **8** likely possesses the ability to penetrate the brain. Additionally, logBB is a standardized measurement of BBB permeability (the logarithmic ratio between the concentration of a compound in the brain and blood), and the logBB values between 0.3 and −1 represent the compound that could pass the BBB[50,51]. The logBB value of compound 8 was predicted as −0.09, which suggests compound **8** possesses the ability to penetrate BBB. Likewise, multiparameter optimization (MPO) is a desirability tool to assess the BBB-permeability of drug candidates. Generally, a CNS MPO score on a scale between 0 and 6, and a score value ≥ 4.0 is highly desirable[52]. The calculated MPO score for compound **8** was 5.3, indicating compound **8** as a potential candidate. Moreover, *ex vivo* measurements[53] of BBB permeability in rat brain tissues and plasma by LC−MS/MS further supported this, demonstrating compound **8** can traverse the BBB (Supporting Information Table S1).

2.3. Radiochemistry

The radiolabeled compound, [¹⁸F]**8**, was designed to be synthesized through S_NAr reactions[54] of the corresponding precursor featuring a nitro leaving group, **22**. Following a synthesis route similar to that of compound **8** but incorporating 2-fluoro-6-nitropyridine (**17**), the reaction steps included substitution, hydrazinolysis, intermolecular cyclization, deprotection, and reductive amination, yielding the compound **22** in 2.5% yield over five steps (Scheme 2). Upon heating with [¹⁸F]TEAF/TEAB at 180 °C for 30 min, the labeling precursor **22** smoothly transformed into [¹⁸F]**8**. Employing an automated synthesis module encompassing radiolabeling, purification, and formulation, [¹⁸F]**8** was obtained with a non-decay-corrected radiochemical yield of $7.9 \pm 2.2\%$ ($n \geq 3$) within 100 min. The product exhibited >95% radiochemical purity and a molar activity >58.8 GBq/μmol (Supporting Information Fig. S1) at the end of synthesis (EOS). The *in vitro* stability of the radiotracer was investigated by incubation at 37 °C in saline containing 10% EtOH (Supporting Information Fig. S2A) or monkey plasma samples (Fig. S2B). As expected, [¹⁸F]**8** was proved to be stable in these media, with

no degradation observed by radio-HPLC up to 120 min of incubation time. The ultrafiltration method showed an unbound free fraction (f_u) of [¹⁸F]V1A-2303 as $34.4 \pm 2.2\%$ using non-human primate (NHP) plasma.

2.4. Cell uptake assay, ex vivo and in vitro autoradiography

To assess the *in vitro* specificity of [¹⁸F]**8** to the V1a receptor, cell uptake studies were conducted. Chinese hamster ovary (CHO) cells expressing the human V1a receptor were incubated with [¹⁸F]**8** alone or in combination with a more than 100-fold excess amount of the non-radioactive compound **8** and V1a antagonists PF-184563, Balovaptan and SRX246 (Fig. 2A). Both structurally similar V1a antagonists (PF-184563, Balovaptan) and structurally different V1a antagonists (SRX246) resulted in a substantial reduction in [¹⁸F]**8** cell uptake, indicating the specific binding of [¹⁸F]**8** to the V1a receptor *in vitro*.

To further explore the binding specificity of [¹⁸F]**8** at tissue levels, *ex vivo* autoradiography studies were performed on liver slices from C57BL/6 mice, and *in vitro* autoradiography studies were conducted on brain sections from rats and adrenal gland sections from monkeys. Under baseline conditions, high signal intensities were observed in liver sections (Fig. 2B). Pretreatment with balovaptan (10 mg/kg, i.v.) led to a roughly 50% reduction in signal intensities (Fig. 2C). For brain slices, while relative signal intensity only decreased by 8.5%, there was a statistically significant difference between the baseline and blocking conditions (Supporting Information Fig. S3). Because the V1a receptor density in the brain is low[55-58] may not be sufficiently high to accurately reflect specific V1a receptor binding in the brain. Furthermore, adrenal gland sections from monkeys incubated with [¹⁸F]**8** exhibited high specific binding in the adrenal cortex (zona glomerulosa and zona fasciculata) and medulla (Fig. 2D), regions known to express the V1a receptor[59]. The signal intensities significantly decreased with the blockade of V1a antagonists V1A-2303 or PF-184563 (10 μmol/L; Fig. 2E). Compared to the blocking studies using unlabeled V1A-2303, the substantial activity retention observed in rhesus monkey adrenals under PF-184563 blocking conditions could be
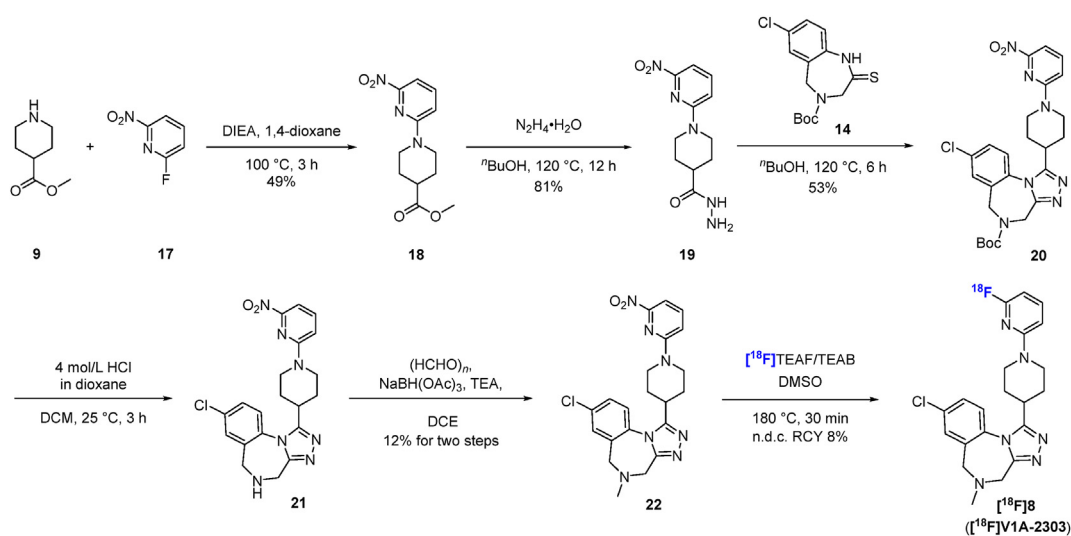
Scheme 2 Synthesis of radiolabeled V1a ligand [¹⁸F]V1A-2303.
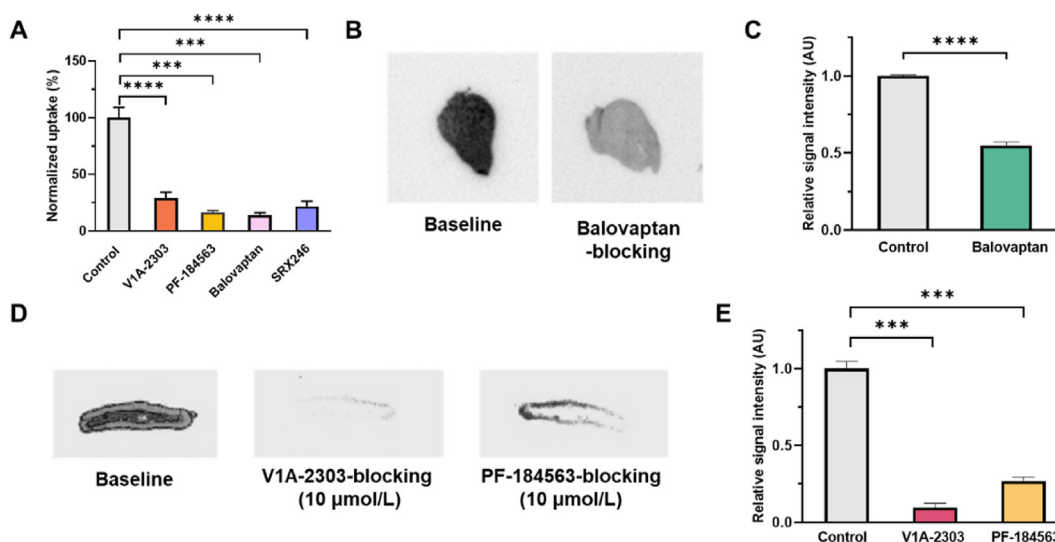
Figure 2 *In vitro* cell uptake assay and autoradiography of [^{18}F]**8**. (A) Normalized uptake ratio of [^{18}F]V1A-2303 in CHO cell line that expresses the human V1a receptor, in the presence of non-radioactive V1A-2303, V1a receptor antagonists PF-184563, balovaptan or SRX246 as blocking agents (0.5 μmol/L); Representative images for baseline and blocking (10 μmol/L) by (B) *ex vivo* autoradiography in mice liver and (D) *in vitro* autoradiography in monkey adrenal; (C, E) Comparative analysis under baseline and blocking conditions to quantitatively assess the specificity of [^{18}F]V1A-2303. All data are shown as mean ± SD ($n \geq 3$) and analyzed by unpaired *t*-test. ***$P < 0.001$, ****$P < 0.0001$.

attributed to the residual nonspecific binding. These findings further demonstrate that [^{18}F]**8** binds specifically to the V1a receptor, and this binding is effectively blocked by various V1a antagonists.

2.5. Biodistribution study in mice

To study the pharmacokinetic profile of [^{18}F]**8**, we assessed its uptake, distribution, and elimination in C57BL/6 mice at five-time points (1, 5, 15, 30, and 60 min) post-injection (p.i.). The results are presented in Fig. 3A and Supporting Information Table S2 as the percentage of the injected dose per gram of wet tissue (%ID/g). The initial clearance of radioactivity from the blood was rapid, exhibiting a clearance ratio of 2.3 between 1 and 60 min. Several organs, including the heart, lung, liver, pancreas, small intestine, and kidney, displayed high radioactivity levels (>5%ID/g) at initial time points. Subsequently, radioactivity rapidly decreased in most tissues, except for the liver, where it initially increased until the 5 min p.i. before gradually diminishing. The radioactivity in the stomach and small intestine plateaued at 30 min p.i., while significant radioactivity persisted in the bladder at 60 min p.i. The relatively elevated uptake in the liver and small intestine may be attributed to hepatobiliary excretion, along with potential intestinal reabsorption. Meanwhile, the relatively constant uptake in the kidneys and gradual accumulation in the bladder suggests renal clearance.

The brain uptake was low at 0.91 %ID/g (SUV = 0.18) at 1 min p.i. and gradually diminishing over 60 min (Fig. 3A and B), likely influenced by P-glycoprotein (P-gp) efflux in mouse brain (Supporting Information Fig. S4). An *ex vivo* brain metabolism study, analyzing radio chromatograms at 5 and 30 min p.i., showed good stability and a modest rate of metabolization of [^{18}F]**8** in the brain (Supporting Information Fig. S5, Tables S3 and S4). The intact parent fractions in the brain were 90.3 ± 1.2% at 5 min and 78.8 ± 0.4% at 30 min, indicating that the majority of brain uptake likely originated from the probe itself rather than its metabolites. However, the *ex vivo* analysis of liver metabolism

revealed that, at 30 min, 26.9 ± 1.69% of the signal in the liver originated from the parent radiotracer, while the remaining 73% corresponded to radio metabolites (Supporting Information Fig. S6). We noted a progressive buildup of radioactivity in bone, suggesting potential defluorination of the tracer in rodents.

When pre-treating with balovaptan (10 mg/kg) before the injection of radiolabeled tracer [^{18}F]**8**, the radioactivity in most organs and tissues decreased at 5 min and 30 min p.i (Supporting Information Fig. S7 and Table S5). The radioactivity in the liver declined by 60% at 5 min and 54% at 30 min (Fig. 3C), while the radioactivity in the kidney declined by 30% at 5 min and 10% at 30 min (Fig. 3D), in the comparison with baseline study. However, the changes without statistical significance in the kidney indicate that the uptake is mainly attributed to excretion rather than binding, while the significant change in the liver may exhibit high binding specificity.

2.6. PET imaging studies of [^{18}F]V1A-2303 in monkey

Dynamic PET imaging studies were conducted in the rhesus monkey's brain to assess brain permeability, binding specificity, and washout kinetics of [^{18}F]**8**. Fig. 4A illustrates the co-registration of averaged PET images of the brain (0−90 min) with the MRI T1-weighted template, and Fig. 4B displays the time-activity curves (TACs) of specific brain regions. The baseline study indicated that [^{18}F]**8** was able to cross the blood−brain barrier, with a peak whole-brain standard uptake value (SUV) of 1.6 at 2.5 min. Radioactivity in all regions of interest exhibited a rapid increase, peaked at 2.5 min, and was gradually washed out over 100 min. Specifically, there was a heterogeneous distribution of radioactivity, with the highest level in the pituitary gland, followed by the thalamus, striatum, amygdala, hippocampus, and cerebellum with the least. In Fig. 4C, static whole-body maximum intensity projection (MIP) images acquired 100−110 min p.i. are presented. There was some radioactivity in the vertebrae and potential joints, suggesting potential defluorination of the tracer in non-human primates (NHPs). Comparing results with and without
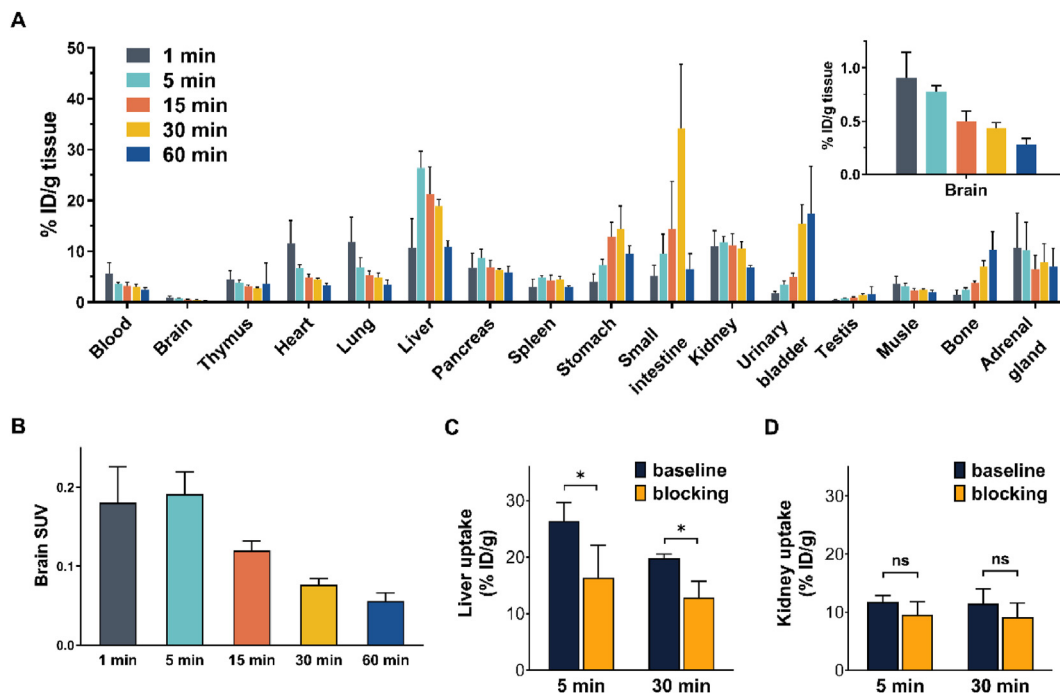
Figure 3 *Ex vivo* biodistribution of [^{18}F]8 in mice. (A) Biodistribution of tracer [^{18}F]8 at five different time points characterized by injected dose per gram of wet tissue (%ID/g) under baseline condition. The inset shows the brain uptake; (B) Standard uptake value (SUV) in the brain at five different time points; and comparison of tracer uptake in the liver (C) and kidney (D) under baseline and blocking conditions. V1a antagonist balovaptan (10 mg/kg) was used as a blocking agent. All data were shown as mean ± standard deviations ($n = 4$) and analyzed by paired *t*-test. [ns]$P > 0.05$, *$P \leq 0.05$.
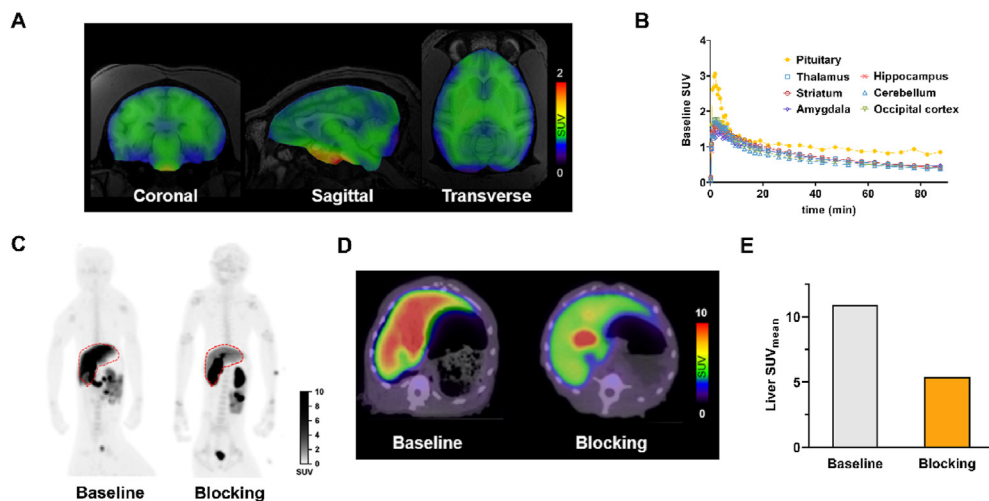
Figure 4 PET imaging studies of [^{18}F]8 in the rhesus monkey. (A) Representative summed PET/MR images (0−90 min) of the brain under baseline conditions; (B) Time-activity curves (TACs) in representative brain regions under baseline conditions; (C) Whole body maximum intensity projection (MIP) images; (D) PET/CT static images (100−110 min) of liver; (E) Liver mean standard uptake value (SUV$_{mean}$) of monkey after 100 min injection under both baseline and blocking conditions. Blocking was pre-treated with balovaptan (3 mg/kg).

pretreatment of balovaptan (3 mg/kg), a notable accumulation was observed in the liver in the baseline, with some activity extending to the intestine, suggesting a preference for hepatobiliary excretion over renal clearance, which was similar to the biodistribution results in rodents. Following pretreatment with balovaptan, a notable reduction in the liver signal was observed, with the SUV in the liver decreasing from 11 to 5 (Fig. 4D and E), indicating a pronounced blockade effect on the hepatic uptake. However, pretreatment with V1a antagonist balovaptan (3 mg/kg) did not decrease the signal in various brain regions, yet resulted in increased radioactivity and a higher whole-brain area under the curve (AUC) (Supporting Information Fig. S8 and Table S6).

2.7. Kinetic modeling in NHP brain

We employed compartmental modeling with a metabolite-corrected input function to determine brain kinetic parameters. Following intravenous bolus injection of $[^{18}F]\mathbf{8}$, plasma radioactivity exhibited a transient peak within 1 min, followed by a substantial decrease (Fig. 5A). The pre-treatment of balovaptan (3 mg/kg) resulted in a slight increase in peak activity and AUC. The plasma-to-whole blood ratio remained relatively stable, averaging around 1.01 ± 0.05 (Supporting Information Fig. S9 and Table S7). $[^{18}F]\mathbf{8}$ exhibited reasonable metabolism in arterial blood, with intact parent fractions of 66.1% at 10 min and 38.6% at 30 min (Fig. 5B). Balovaptan pre-treatment slightly elevated the intact parent fraction (74.4% at 10 min and 47.5% at 30 min), indicating increased plasma availability of the tracer induced by balovaptan. This observation aligns with the hypothesis that balovaptan exerts a more extensive blockade effect on peripheral receptors than in the brain. As illustrated in Fig. 5C and Supporting Information Table S8, radio-chromatogram analyses revealed that $[^{18}F]\mathbf{8}$ had a retention time of 10 min. The primary polar radioactive metabolite exhibited a shorter retention time, implying a reduced likelihood of penetrating the BBB compared to the parent tracer.

The representative kinetic modeling results, along with detailed parameters obtained from various fitting models for all volumes of interest (VOIs), are summarized in Table 2. The two-compartment model (2TCM) consistently outperformed the one-compartment model (1TCM) for all evaluated VOIs, evident from the lower Akaike Information Criterion (AIC) (Fig. 5D). Under baseline conditions, the amygdala exhibited the highest total volume of distribution (V_T) of 1.26, followed by the thalamus, striatum, and hippocampus, with the cerebellum displaying the lowest V_T. Under blocking condition, administration of V1a antagonist balovaptan (3 mg/kg) before tracer injection enhanced the V_T values of analyzed brain regions and indicated an absence of specific binding in the brain. Fig. 5E illustrates the Logan plot for the striatum, highlighting a robust correlation between V_T

values derived from 2TCM and Logan plots (Pearson's $r = 0.941$, $P < 0.0001$, Supporting Information Fig. S10). Furthermore, Supporting Information Table S9 outlines the V_T values for each brain region across five different time intervals, ranging from 0 to 60 to 0−100 min p.i. The stability of V_T in the thalamus and striatum is depicted in Fig. 5F. During the 60−100 min interval, V_T values calculated using 2TCM fitting exhibited minimal fluctuation, remaining between 90% and 100%. This consistency suggests that V_T stabilizes after 60 min in the dynamic PET imaging scans. These results suggest that 2TCM constitutes a suitable model for the assessment of $[^{18}F]\mathbf{8}$ kinetic parameters in the NHP brain.

V1a receptor plays a critical role in the regulation of a range of physiological processes, and its dysregulation influences the pathophysiology of various neurological conditions, social cognition and behavior. Moreover, the impact of the V1a receptor extends beyond the CNS to numerous peripheral pathologies, including metabolic regulation, blood pressure, and vascular resistance. Recent studies have also considered the V1a receptor as a potential therapeutic target for castration-resistant prostate cancer. The wide-ranging physiological impacts of the V1a receptor highlight its potential as a therapeutic target for both central and peripheral diseases.

V1A-2303 was designed and synthesized as a V1a receptor-targeted ligand. *In vitro* pharmacological characterization revealed an IC_{50} of 2.33 nmol/L and a K_i of 0.46 nmol/L for hV1a, a $\log D_{7.4}$ of 1.81, and an ER of 0.85. Balovaptan[42], for comparison, exhibited a K_b of 0.23 nmol/L for hV1a, a $\log D_{7.4}$ of 3.2, and a hP-gp efflux ratio of 2.3. Additionally, the binding affinity of V1A-2303 is higher than the other V1a-targeted radio ligands reported in the literature. Based on these pharmacological parameters, V1A-2303 can be considered a V1a receptor-targeted ligand similar to balovaptan.

In the biodistribution study in mice, a low brain uptake (0.91 % ID/g, SUV = 0.18 at 1 min p.i.) indicated poor brain permeability. However, moderate brain uptake was observed in PET imaging of rhesus monkeys (SUV = 1.6 at 2.5 min p.i.), approximately 8-
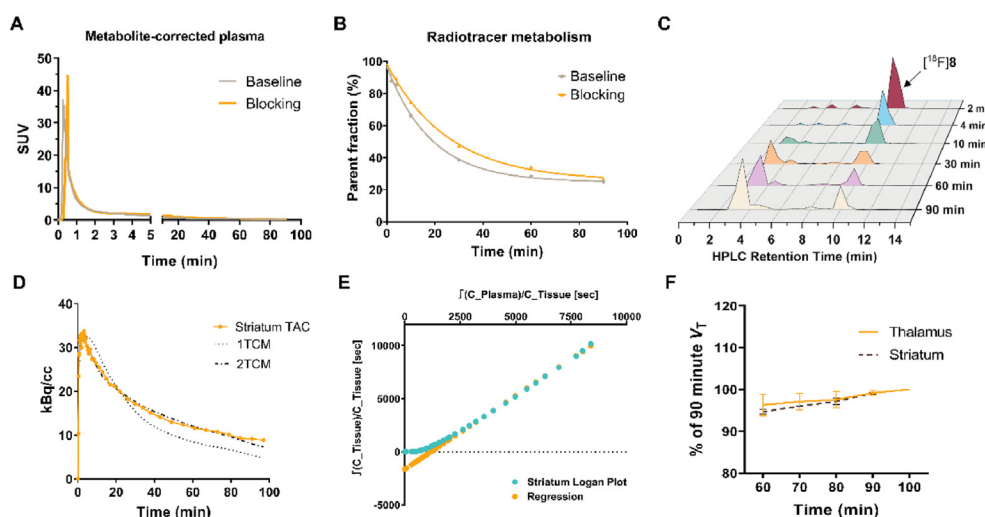
Figure 5 Plasma data, kinetic modeling, and time stability analysis in the brains of non-human primates (NHPs). (A) Individual metabolite-corrected $[^{18}F]$V1A-2303 standard uptake value (SUV) time courses in plasma; (B) Individual fraction of unchanged parent compound over time; (C) Representative radio-chromatograms of plasma samples under baseline conditions; (D, E) Model fits of one-tissue compartment model (1TCM), two-tissue compartment model (2TCM), and Logan plot on the baseline scan of monkey striatum. (F) Estimation of total volume of distribution (V_T) calculated for 60−100 min scan windows in 10 min increments compared to the final 90 min V_T for the thalamus and striatum.

Table 2 Pharmacokinetic parameters estimated from different fitting models.

Region	K_1 (mL/cm^3/min)	k_2 (/min)	k_3 (/min)	k_4 (/min)	V_T (mL/cm^3)	V_T (block)[a]
2TCM						
Thalamus	0.10 ± 0.03	0.15 ± 0.03	0.05 ± 0.01	0.09 ± 0.05	1.14 ± 0.35	1.95
Striatum	0.09 ± 0.03	0.15 ± 0.03	0.04 ± 0.02	0.05 ± 0.002	1.11 ± 0.32	1.86
Occipital cortex	0.10 ± 0.02	0.21 ± 0.01	0.03 ± 0.0002	0.02 ± 0.01	1.10 ± 0.47	1.53
Amygdala	0.09 ± 0.04	0.15 ± 0.05	0.03 ± 0.02	0.02 ± 0.002	1.26 ± 0.42	1.73
Hippocampus	0.09 ± 0.04	0.16 ± 0.06	0.03 ± 0.02	0.03 ± 0.01	1.13 ± 0.31	1.68
Cerebellum	0.10 ± 0.03	0.23 ± 0.03	0.04 ± 0.001	0.03 ± 0.01	0.97 ± 0.39	1.48
1TCM						
Thalamus	0.09 ± 0.02	0.09 ± 0.004			0.99 ± 0.21	1.93
Striatum	0.08 ± 0.02	0.09 ± 0.005			0.93 ± 0.22	1.78
Occipital cortex	0.09 ± 0.01	0.14 ± 0.01			0.65 ± 0.71	1.34
Amygdala	0.07 ± 0.03	0.08 ± 0.01			0.87 ± 0.23	1.62
Hippocampus	0.08 ± 0.03	0.09 ± 0.01			0.82 ± 0.19	1.60
Cerebellum	0.08 ± 0.02	0.13 ± 0.007			0.61 ± 0.18	1.36
Logan plot						
Thalamus					1.18 ± 0.36	1.96
Striatum					1.14 ± 0.34	1.88
Occipital cortex					1.10 ± 0.43	1.54
Amygdala					1.33 ± 0.55	1.69
Hippocampus					1.16 ± 0.38	1.71
Cerebellum					1.03 ± 0.41	1.53

Data are presented as mean ± SD.

[a]Pre-blocking studies were performed with 3 mg/kg of balovaptan.

fold higher than in mice. This significant difference is likely attributed to species variations in efflux transporter expression in the brain, as the expression of the efflux transporter MDR1 was 2.33-fold lower in humans than in mice[60]. While mice studies are an important step in the development of CNS-targeted tracers, it is crucial to remember that they do not always accurately predict efficacy in higher species. Further research in NHP models and even humans is necessary to fully evaluate their properties.

[18F]**8** exhibits good stability and reasonable metabolization rates. In the *ex vivo* brain metabolism study, intact parent fractions of [18F]**8** were 90.3 ± 1.2% at 5 min and 78.8 ± 0.4% at 30 min. Pharmacokinetic results, brain tissue distribution study, and radiochromatogram analyses supported that the majority of brain uptake in biodistribution and PET imaging studies likely originated from the probe itself rather than its metabolites. In kinetic modeling, intact parent fractions of [18F]**8** in plasma were 66.1% at 10 min and 38.6% at 30 min, comparable to [18F]LW223[61] (a TSPO-targeted PET radioligand, ~50% at 10 min and ~40% at 30 min) and superior to ^{18}F-AV45[62] (the first FDA-approved commercial radiotracer for Aβ PET imaging, 35 ± 10% at 10 min and 14.4 ± 7.3% at 30 min). Consequently, blood data from monkey experiments suggests modest metabolization of [18F]**8**.

In the PET imaging studies of [18F]**8** in monkeys, pretreatment with V1a antagonist balovaptan notably decreased the signal in the liver, but did not decrease the signal in various brain regions. The SUV in the pituitary (Fig. 4B and Supporting Information Fig. S8) showed a slight increase at both 10 min (from 1.25 to 1.30) and 30 min (from 0.91 to 1.03) compared to the non-pretreated group. The AUC (0−90 min) value of the time-activity curve of metabolite-corrected pituitary increased by 5.9%. The increase caused by the pretreatment with balovaptan can be attributed to three factors: 1) The increased radioactivity in plasma. On one hand, the peak SUV in the metabolite-corrected plasma (Fig. 5A) is 37.11 at 0.267 min in baseline and 44.52 at 0.517 min (an 18.9%

increase) in blocking. On the other hand, the area (Supporting Information Table S10) under the metabolite-corrected plasma time−activity curve (0−90 min) increased by 20% (from 57.04 to 68.40); 2) The increased metabolic stability of [18F]**8**. As shown in Fig. 5B, the pre-treatment of balovaptan increased the intact parent fraction in plasma by 12.6% at 10 min and 23.2% at 30 min; 3) The increased unbound free fraction (f_u or f_p). This factor is directly related to the ability of the radioligand to cross the blood-brain barrier and bind to its target. It was reported that the mean f_p value of blocked scans was likely higher than that of baseline scans[63]. As previously discussed, the administration of the blocking agent altered the intact parent fraction in plasma, which showed higher concentrations of [18F]**8** compared to baseline, likely due to the displacement of the radioligand from peripheral binding sites. This suggests that f_u or f_p may be significantly increased in the presence of pharmacological dose of blocker.

PET is a promising tool for studying complex physiological and pathological mechanisms, and the development of innovative PET tracers holds the potential to improve diagnostics, personalize treatment approaches, and advance our comprehension of various diseases. A prime example is the development of TSPO radioligands. The latest radioligands are insensitive to the rs6971 polymorphism, which significantly alters the affinity of TSPO for drug and probe, and enables the visualization of *in vivo* preclinical brain inflammation. This example sets the stage for further investigations of the V1a receptor. Similarly, the single nucleotide polymorphisms (rs11174811) and microsatellite polymorphisms (RS1 and RS3)[26,64-66] of V1a, associated with autism, pair bonding-behavior, maternal behavior, and other aspects of social cognition and behavior, may shed light on individual differences in social behavior and heritable disorders. Hence, the ongoing development of novel PET ligands targeting the V1a receptor is crucial for unraveling the complexities of physiological and pathological processes, especially in regulating of social,

emotional, and cognitive behaviors. Such progress will facilitate the translation of findings from animal studies on prosocial behavior to preclinical human research.

3. Conclusions

We synthesized [^{18}F]V1A-2303 ([^{18}F]**8**), a PET ligand for the V1a receptor. [^{18}F]**8** exhibited favorable pharmacological characteristics, including high binding affinity ($K_i = 0.46$ nmol/L), excellent selectivity (>100-fold for V1a over other AVP receptors), and efficient BBB permeability. Autoradiography and biodistribution studies demonstrated good specificity for the V1a receptor in peripheral tissues. [^{18}F]**8** also showed high specific binding in the liver and was able to cross the BBB in NHPs as determined by PET imaging. However, kinetic modeling using a metabolite-corrected arterial input function revealed a lack of specific binding in the brain. Further medicinal chemistry efforts are underway and we aim to increase binding affinity in 10−30-fold based on our brain-penetrant ligand scaffold and test if moderate specific binding could be achieved under these conditions to enable V1a imaging in the CNS.

4. Experimental

4.1. Reagents

Unless otherwise indicated, all reagents were acquired from Sigma−Aldrich and solvents were newly dried and degassed before use.

4.2. Animals

Sprague−Dawley (SD) rats (male, 7−8 weeks, 220−240 g) were purchased from Charles River Laboratory, and C57BL/6 mice (male, 7−8 weeks, 20−25 g) were purchased from GuangDong GemPharmatech Co., Ltd. All animals received humane care and were housed in cages with a 12 h light/dark schedule. In compliance with Jinan University's Animal Ethics Committee, the rodent experiment protocols have been approved. Several studies on rhesus monkeys (male, six years old, 6−7 kg) were approved by the Institutional Animal Care and Use Committee (IACUC) of Guangdong Landau Biotechnology Co., Ltd. This organization is accredited by the Association for Assessment and Accreditation of Laboratory Animal Care (AAALAC).

4.3. Chemical synthesis

Details of synthesis procedures and NMR data are included in the Supporting Information.

4.4. Pharmacology and ADME properties

4.4.1. Binding affinity and selectivity assays for V1A-2303 (8)
All pharmacology studies were performed at Eurofins BioPharma Services. In vitro inhibitory effects of compound V1A-2303 on V1a, V1b, and V2 receptors were determined using established commercial assays. Reference standards were included in every assay to verify the accuracy of the results. The determination of IC$_{50}$ values was conducted through a non-linear, least squares regression analysis employing MathIQTM (ID Business Solutions Ltd., UK). In cases where inhibition constants (K_i) were reported, the K_i values were calculated using the Cheng and Prusoff equation[67]. The presentation of IC$_{50}$ and K_i values does not include the Standard Error of the Mean (SEM).

General experimental procedure (V1A assays as an example): Human recombinant vasopressin V1A receptors expressed in HEK-293 cells are used in modified Tris-HCl buffer pH 7.4. A 0.26 μg aliquot is incubated with 0.03 nmol/L [^{125}I]phenylacetyl-D-Tyr(Me)-Phe-Gln-Asn-Arg-Pro-Arg-Tyr-NH$_2$ for 120 min at 25 °C. Non-specific binding is estimated in the presence of 1 μmol/L [Arg8]vasopressin. Receptors are filtered and washed, the filters are then counted to determine [^{125}I]phenylacetyl-D-Tyr(Me)-Phe-Gln-Asn-Arg-Pro-Arg-Tyr-NH$_2$ specifically bound.

4.4.2. Measurement of lipophilicity
[^{18}F]V1A-2303 was formulated into a 15 mL tube containing n-octanol (3.65 mL, 3 g) and PBS (3 mL, 3 g) that were pre-saturated. When the vortex has been vortexing for 3 min, for better liquid layering, the hybrid was divided into three new tubes and separated by centrifugation for 5 min (3500 rpm). In the following steps, every aliquot's count per min (CPM) was determined using an automatic gamma counter (WIZARD2 2480, PerkinElmer, USA), and decay and background corrections were made. To calculate log$D$, we divided the radioactivity between the organic phase and the aqueous phase.

4.4.3. MDCK-MDR1 experiment
In vitro brain permeability of V1A-2303 was carried out using a Madin Darby canine kidney (MDCK) cells with the MDR1 gene model by methods[68]. Reference compounds are digoxin (a P-glycoprotein drug efflux transporter control), metoprolol (a high permeable control), atenolol (a low permeable control), and Lucifer Yellow. Hank's balanced salt solution (HBSS) buffer along with 5 mmol/L Lucifer Yellow and 0.4% DMSO (pH 7.4) was used to wash MDR1-MDCK cells twice before transport experiments.

4.4.4. Ex vivo permeability of BBB in SD rats
These studies were performed at ChemPartner. SD rats (220−240 g, male, $n = 9$) were administered intravenously at a dose of V1A-2303 (0.03 mg/kg) via foot dorsal vein injection. At the time points of 5, 30, and 60 min, a blood sample of nearly 150 μL was collected from the animal. Immediately following collection, the blood samples were kept on ice and centrifuged (2000×g, 4 °C, 5 min) to obtain plasma. As soon as the animals had been anesthetized and exsanguinated, tissue samples (pituitary, brainstem, hippocampus, striatum, and cortex) were collected, rinsed with pre-cooled saline, dried on filtrate paper, weighed, and frozen on dry ice. Tissue samples were homogenized with 3 volumes (v/w) of homogenizing solution (PBS) before analysis. The concentrations of V1A-2303 in samples were quantified through liquid chromatography-tandem mass spectrometry (LC−MS/MS-39, Triple Quad 6500+). The detection of all analytes was carried out in positive ionization mode. The MRM (multiple reaction monitoring) transitions were m/z 413.10 → 177.20 for V1A-2303 and m/z 230.00 → 121.00 for Osalmid (internal standard).

4.5. Radiochemistry

[^{18}F]Fluoride was generated via the ^{18}O(p,n)^{18}F reaction in a 10 MeV cyclotron (GE, Qilin) using >98% enriched H$_2$^{18}O (Taiyo Nippon Sanso Corporation, Tokyo, Japan). [^{18}F]Fluoride was trapped with a Sep-Pak QMA cartridge (Waters, 186004540), and

eluted with TEAHCO$_3$ (2.0 mg) in MeOH (1 mL). After an azeotropic drying, precursor **22** (0.5 mg) in anhydrous DMSO (500 μL) was added. The radiosynthesis occurred at 180 °C for 30 min, and was followed by HPLC purification with an Osaka Soda CAPCELL PAK C18 column (UG80, 5 μm, 10 mm i.d. × 250 mm) using a mobile phase of CH$_3$CN/H$_2$O (*v/v*, 45/55) containing 0.1% Et$_3$N and at 3.0 mL/min. The retention time (*t*$_R$) of [18F]**8** was 18.0 min. The product fraction was collected, diluted with water, and trapped with a C-18 light cartridge (Waters, WAT023561). Eluted with 1 mL EtOH and diluted with 9 mL saline, the final product was obtained. Analytical HPLC, with a GL Sciences WondaSil C18-WR column (4.6 mm × 150 mm) and the same mobile phase at a flow rate of 1 mL/min (*t*$_R$: 6.7 min), confirmed the identity of [18F]**8** by co-injection with the reference compound **8**.

4.6. Cell uptake studies

The CHO-V1a cell line, expressing the Human V1a Receptor, was cultured in Ham's F12 medium (Life Technologies) with 10% fetal bovine serum (Corning), 1% penicillin-streptomycin (Life Technologies) and Geneticin (G418, 0.4 mg/mL, Life Technologies). Maintained at 37 °C with 5% CO2 and high humidity, subpassaging involved a 1:3 split using 0.25% trypsin/0.02% EDTA. For cell uptake, CHO-V1a cells were plated at 2×10^5 cells/well for 24 h, exposed to [18F]V1A-2303, and incubated for 60 min. After PBS washes, cells were harvested with 0.1 mol/L NaOH. The blocking assay included a nonradioactive reference or PF-184563, Balovaptan, and SRX246 incubated for 60 min. Gamma counter measurements assessed cell uptake (% AD). Data represent averages from quadruplicate wells.

4.7. In vitro stability and f$_u$ in plasma

The *in vitro* stability of [18F]V1A-2303 was investigated by incubation at room temperature in saline containing 10% EtOH or monkey plasma for 0, 1 and, 2 h. Radioactivity in the mixture was detected by analytical HPLC.

The unbound fraction of [18F]V1A-2303 in NHP plasma samples was determined using an ultrafiltration method[69]. Arterial blood (2.5 mL) was drawn from the monkey, then centrifuged (5 min, 14,000 rpm, 4 °C) to obtain plasma. We added a solution of [18F]V1A-2303 (185 kBq) quadruplicately to the plasma (150 μL). Each tube was incubated for 10 min at 37 °C and then added with 300 μL cold PBS (pH 7.4) and vortexed for 15 s. We centrifuged the 460 μL mixture in a centrifuge tube containing an Amicon® Ultra-0.5 mL device (Merck Millipore Ltd. Tullagreen, Carrigtwohill, Co. Cork, IRELAND) for 20 min (14,000×g, 4 °C). To get the concentrated solution, the filter was removed and inverted into a new tube, and centrifuged again (1000×g for 2 min at 4 °C). Each section of the sample was measured using an automatic gamma counter (WIZARD2 2480, PerkinElmer, USA). The f$_u$ value was calculated as Eq. (1):

$$f_u \ (\%) = 1 - (\text{CPM of filter membrane}) / [(\text{CPM of filter solution}) + (\text{CPM of concentrated solution}) + (\text{CPM of filter membrane})] \times 100 \tag{1}$$

4.8. Autoradiography of ex vivo in mice liver and in vitro in monkey adrenal

[18F]V1A-2303 (7.4 MBq per animal) was administered intravenously *via* the tail vein to one group of C57BL/6 mice (male, 8

weeks, 25 g, $n = 3$). In another group, to determine the receptor-specific binding in the liver, mice were pretreated with balovaptan (10 mg/kg, i.v.) before the injection of tracer. Cervical dislocation was performed 30 min p.i. to sacrifice mice. After the liver parts were immediately removed, they were embedded in Tissue-Tek® (O.C.T.). Liquid nitrogen was used to freeze the tissue, and 20 μm sections were cut using a cryotome. A 12-h exposure to a phosphor imager plate followed.

Several sections of monkey adrenal tissue from cynomolgus macaques (male, $n = 3$) were stored at −80 °C until further processing. Briefly, sections were preconditioned with 200 mL buffer1 (50 mmol/L Tris containing 0.1% BSA) in a reservoir for 10 min. Afterward, incubation of the sections with 200 mL [18F]V1A-2303 solution (37 kBq/mL in buffer1) for 1 h was conducted. For baseline conditions, sections were dipped into the above solution and 10 μmol/L DMSO. For blockade, 10 μmol/L of V1a receptor antagonist, PF-184563, was added. In the following step, sections were transferred to buffer 2 (50 mmol/L Tris without 0.1%BSA) and washed. A 12-h exposure to a phosphor imager plate followed.

Imaging plates (BAS-MS2025, GE Healthcare, NJ, USA), an imager (Amersham Typhoon, Cytiva, USA), and a Bio-Imaging Analyzer System (Multi Gauge Version 2.3, FUJIFILM) were used to obtain autoradiograms and measure photostimulated luminescence (PSL) values in ROIs.

4.9. Biodistribution studies in mice

In this study, C57BL/6 mice (male, 7 weeks, 20−25 g) were used. *Via* the tail vein, each mouse received the solution of [18F]V1A-2303 (3.7 MBq/100 μL). At each time point (1, 5, 15, 30, and 60 min) p.i., four mice were dissected to get a whole brain, thymus, heart, lungs, liver, pancreas, spleen, stomach, small intestine, kidneys, bladder, testes, muscle, bone, adrenal gland, and blood. These organs were placed into glass tubes and weighed. A 2480 Wizard automatic gamma counter (PerkinElmer, USA) was used to determine how much radioactivity was reserved in them. A percentage of the %ID/g was shown to indicate the radioactivity concentration[70].

4.10. Measurement of [18F]8 radio-metabolites in the brain and plasma of rats

SD rats (male, 7−8 weeks, 220−240 g) were injected with [18F]**8** (37 MBq per animal) *via* the tail vein and decapitated at 5 and 30 min ($n = 3$, each time point) later. The blood and brain were collected and processed for analysis. The rat brain was homogenized in 50% CH$_3$CN on ice and then centrifuged for 2.5 min at 4 °C (14,500×g). All blood samples were centrifuged at 6000 rpm for 5 min to get the upper plasma. The plasma samples were extracted and placed in CH$_3$CN to sediment protein by centrifugation at 14,000 rpm for 3 min V1A-2303 standard was added to the above supernatant, and the mixture was separated into glass tubes at intervals of 30 s using semipreparative HPLC. Analyses were performed at room temperature (column OSAKA SODA CAPCELL PAK C18 UG80 5 μm, 10 mm × 250 mm) using a mobile phase of CH$_3$CN/H$_2$O (*v/v*, 50/50) containing 0.1% Et$_3$N and at 3.0 mL/min. The radioactivity of separated samples was detected with the WIZARD2 2480 automatic gamma counter (PerkinElmer, USA). The unmetabolized [18F]**8** parent fraction was determined as the ratio of the sum of radioactivity in fractions containing the parent compound to the total amount of radioactivity collected.

4.11. *In vivo PET brain imaging of mice under baseline and P-glycoprotein (P-gp) blocking conditions*

Each mouse was anesthetized by 2% isoflurane inhalation and an intravenous catheter was inserted into the tail vein. The radiotracer [^{18}F]**8** (*ca.* 5 MBq/150−200 μL) was injected into the mouse *via* the preinstalled catheter, and the 60 min dynamic acquisition of PET signals in the mouse brain was started at the same time. PET/CT imaging experiments were performed on an IRIS small animal PET/CT imaging system (Inviscan SAS, Strasbourg, France). To study the influence of P-glycoprotein (P-gp) on the brain uptake of the tracer, mice received an intravenous injection of cyclosporin (25 mg/kg) in saline (300 μL) containing 10% ethanol and 5% Tween® 80 at 15 min *via* the tail vein catheter before the tracer injection.

PET data were reconstructed with a three-dimensional ordered-subset expectation-maximizaton (3D-OSEM) algorithm with a Monte-Carlo based accurate detector model. PET images were then summed and co-registered with the mouse brain MRI template by PMOD software (version 4.1). The time−activity curve (TAC) was acquired from the volume of interest (VOI) in the whole brain. The radioactivity was decay-corrected to the injection time and expressed as the standardized uptake value (SUV) which was normalized to the injected radioactivity and body weight. The area under the time−activity curve (AUC) was also calculated using the SUV on the TAC from 0 to 60 min.

4.12. *PET imaging studies of [^{18}F]V1A-2303 in monkey*

Before the PET imaging study, rhesus monkeys were restrained from food for 12−15 h. Three male rhesus monkeys (weight range 6−7 kg) underwent a PET scan. The monkey lay on the scanning bed in the supine position and was anesthetized with a mixture of isoflurane and oxygen. After that, the monkey received a saline solution of [^{18}F]V1A-2303 (111−148 MBq) and was followed by a dynamic PET scan of the head for 90 min. For blockade, 3 mg/kg of V1a receptor antagonist, balovaptan, was injected 5 min before [^{18}F]V1A-2303.

To get accurate anatomical orientation of the monkey brain, each monkey was scanned by 3.0 T discovery MR 750 (GE Discovery 750, Milwaukee, USA) with a 3D Bravo T1 sequence (ketamine was injected intramuscularly into a rhesus monkey to make it stay anesthetized during the scan). Then, each monkey has its own T1-weighted MR image of brain as a template to co-register with PET.

Co-registration of PET and T1-weighted MR anatomical images was performed based on the literature method[71]. In this study, 3D T1-weighted MR images were segmented to determine the specific brain regions. We calculated the SUV based on the volumes of different brain regions.

4.13. *Whole blood, plasma activity, and parent fraction of [^{18}F] V1A-2303*

A total of 25 arterial blood samples were collected during the 100 min PET scan of NHPs at 0, 5, 10, 15, 20, 25, 30, 40, 50, 60, 75, 90, 105, 120, 150, 180, 210 and 240 s followed by 10, 20, 30, 45, 60, 75 and 90 min (2.0 mL for 2, 4, 10, 30, 60 and 90 min; the rest are 0.5 mL). The blood samples were quickly transferred to centrifuge tubes that had been rinsed with iced heparin and centrifuged (5 min, 6000 rpm, 4 °C) to obtain plasma. Then, we measured the radioactivity of each 100 μL of plasma and whole blood to get time−activity curves. A radioactive decay correction had been applied to all data from the injection time. We used the metabolite-corrected arterial plasma curve as input function. In order to analyze radio-metabolites, the upper plasma (collected at 2, 4, 10, 30, 60, and 90 min) was deproteinized with acetonitrile by centrifugation (3 min, 14,000 rpm, 4 °C). V1A-2303 standard was added to the above supernatant, and the mixture was separated into glass tubes at intervals of 30 s using semipreparative HPLC. The radioactivity of separated samples was detected with the WIZARD2 2480 automatic gamma counter (PerkinElmer, USA). [^{18}F]V1A-2303 parent fraction was computed as a percent of the overall radioactivity (metabolites and parent).

4.14. *Image data analysis*

The T1-weighted MR anatomical image of the individual monkey, obtained using a 3.0 T discovery MR 750, was co-registered with the PET image using PMOD 4.1 (PMOD technology, Switzerland) software. This was done to analyze the imaging data within specific VOIs and to generate regional TACs. Regional V_T and the kinetic rate constants (K) were calculated for the extracted TACs by reversible one-(1T) and two-(2T) tissue compartment model and Logan graphical analysis with the metabolite-corrected arterial PL input function.

4.15. *V_T time stability analysis*

To assess the temporal stability of V_T, data were progressively trimmed from 100 to 60 min and the corresponding V_T values were normalized to the end-of-scan value at 100 min. V_T was estimated from each truncated data set and normalized to the V_T estimated from the full data set. Normalized V_T that stabilizes within the range of 90%−110% is considered acceptable.

4.16. *Statistical analysis*

The AIC was employed to determine the optimal compartment model[72], with lower AIC values indicating greater model parsimony. Furthermore, Pearson correlation analysis was conducted to assess the relationships between V_T estimated by the 2TCM and the Logan Plot. Statistical significance was defined as a *P*-value less than 0.05. GraphPad Prism (version 9.5.1) was utilized for all statistical analyses. Continuous variables were reported as mean ± standard deviation (SD).

Author contributions

Junqi Hu: Investigation, Writing − original draft. Yinlong Li: Conceptualization, Data curation. Chenchen Dong: Data curation, Formal analysis, Validation. Huiyi Wei: Formal analysis, Methodology. Kai Liao: Validation. Junjie Wei: Resources. Chunyu Zhao: Formal analysis. Ahmad Chaudhary: Data curation. Jiahui Chen: Formal analysis. Hao Xu: Funding acquisition, Conceptualization. Ke Zhong: Writing − review & editing. Steven H.

Liang: Supervision, Writing − review & editing. Lu Wang: Funding acquisition, Supervision. Weijian Ye: Funding acquisition, Supervision, Writing − original draft, Writing − review & editing.

Conflicts of interest

The authors declare no conflicts of interest.

Appendix A. Supporting information

Supporting information to this article can be found online at https://doi.org/10.1016/j.apsb.2024.05.033.

References

1. Sparapani S, Millet-Boureima C, Oliver J, Mu K, Hadavi P, Kalostian T, et al. The biology of vasopressin. *Biomedicines* 2021;**9**: 89.
2. Aikins AO, Nguyen DH, Paundralingga O, Farmer GE, Shimoura CG, Brock C, et al. Cardiovascular neuroendocrinology: emerging role for neurohypophyseal hormones in pathophysiology. *Endocrinology* 2021;**162**:bqab082.
3. Koshimizu TA, Nakamura K, Egashira N, Hiroyama M, Nonoguchi H, Tanoue A. Vasopressin V1a and V1b receptors: from molecules to physiological systems. *Physiol Rev* 2012;**92**:1813−64.
4. Koshimizu TA, Nasa Y, Tanoue A, Oikawa R, Kawahara Y, Kiyono Y, et al. V1a vasopressin receptors maintain normal blood pressure by regulating circulating blood volume and baroreflex sensitivity. *Proc Natl Acad Sci U S A* 2006;**103**:7807−12.
5. Fujiwara Y, Tanoue A, Tsujimoto G, Koshimizu TA. The roles of V1a vasopressin receptors in blood pressure homeostasis: a review of studies on V1a receptor knockout mice. *Clin Exp Nephrol* 2011;**16**: 30−4.
6. Fernández-Varo G, Oró D, Cable EE, Reichenbach V, Carvajal S, de la Presa BG, et al. Vasopressin 1a receptor partial agonism increases sodium excretion and reduces portal hypertension and ascites in cirrhotic rats. *Hepatology* 2015;**63**:207−16.
7. Randesi M, Levran O, Correa da Rosa J, Hankins J, Rule J, Kreek MJ, et al. Association of variants of arginine vasopressin and arginine vasopressin receptor 1a with severe acetaminophen liver injury. *Cell Mol Gastroenter* 2017;**3**:500−5.
8. Zhao N, Peacock SO, Lo CH, Heidman LM, Rice MA, Fahrenholtz CD, et al. Arginine vasopressin receptor 1a is a therapeutic target for castration-resistant prostate cancer. *Sci Transl Med* 2019;**11**:eaaw4636.
9. Liu H, Yu L, Yang L, Green MS. Vasoplegic syndrome: an update on perioperative considerations. *J Clin Anesth* 2017;**40**:63−71.
10. Fernández-Varo G, Jiménez W, Cable E, Ginès P, Harris G, Bukofzer S. Partial vasopressin 1a receptor agonism reduces portal hypertension and hyperaldosteronism and induces a powerful diuretic and natriuretic effect in rats with cirrhosis and ascites. *Biomed Pharmacother* 2023;**165**:115116.
11. Winslow JT, Insel TR. Neuroendocrine basis of social recognition. *Curr Opin Neurobiol* 2004;**14**:248−53.
12. Rauen K, Trabold R, Brem C, Terpolilli NA, Plesnila N. Arginine vasopressin V1a receptor-deficient mice have reduced brain edema and secondary brain damage following traumatic brain injury. *J Neurotrauma* 2013;**30**:1442−8.
13. Dumais KM, Veenema AH. Vasopressin and oxytocin receptor systems in the brain: sex differences and sex-specific regulation of social behavior. *Front Neuroendocrinol* 2016;**40**:1−23.
14. Yang C, Zhang X, Gao J, Wang M, Yang Z. Arginine vasopressin ameliorates spatial learning impairments in chronic cerebral hypoperfusion *via* V1a receptor and autophagy signaling partially. *Transl Psychiat* 2017;**7**:e1174.

15. Dantzer R, Bluthe RM, Koob GF, Le Moal M. Modulation of social memory in male rats by neurohypophyseal peptides. *Psychopharmacology* 1987;**91**:363−8.
16. Everts HG, Koolhaas JM. Differential modulation of lateral septal vasopressin receptor blockade in spatial learning, social recognition, and anxiety-related behaviors in rats. *Behav Brain Res* 1999;**99**: 7−16.
17. Engelmann M, Landgraf R. Microdialysis administration of vasopressin into the septum improves social recognition in Brattleboro rats. *Physiol Behav* 1994;**55**:145−9.
18. Landgraf R, Gerstberger R, Montkowski A, Probst JC, Wotjak CT, Holsboer F, et al. V1 vasopressin receptor antisense oligodeoxynucleotide into septum reduces vasopressin binding, social discrimination abilities, and anxiety-related behavior in rats. *J Neurosci* 1995; **15**:4250−8.
19. Hammock EAD, Lim MM, Nair HP, Young LJ. Association of vasopressin 1a receptor levels with a regulatory microsatellite and behavior. *Genes Brain Behav* 2005;**4**:289−301.
20. Bielsky IF, Hu S-B, Ren X, Terwilliger EF, Young LJ. The V1a vasopressin receptor is necessary and sufficient for normal social recognition: a gene replacement study. *Neuron* 2005;**47**:503−13.
21. Veenema AH, Bredewold R, De Vries GJ. Vasopressin regulates social recognition in juvenile and adult rats of both sexes, but in sex- and age-specific ways. *Horm Behav* 2012;**61**:50−6.
22. Kim SJ, Young LJ, Gonen D, Veenstra-VanderWeele J, Courchesne R, Courchesne E, et al. Transmission disequilibrium testing of arginine vasopressin receptor 1A (AVPR1A) polymorphisms in autism. *Mol Psychiatry* 2002;**7**:503−7.
23. Yirmiya N, Rosenberg C, Levi S, Salomon S, Shulman C, Nemanov L, et al. Association between the arginine vasopressin 1a receptor (*AVPR1a*) gene and autism in a family-based study: mediation by socialization skills. *Mol Psychiatry* 2006;**11**:488−94.
24. Yang SY, Cho SC, Yoo HJ, Cho IH, Park M, Yoe J, et al. Family-based association study of microsatellites in the 5′ flanking region of AVPR1A with autism spectrum disorder in the Korean population. *Psychiatry Res* 2010;**178**:199−201.
25. Tansey KE, Hill MJ, Cochrane LE, Gill M, Anney RJ, Gallagher L. Functionality of promoter microsatellites of arginine vasopressin receptor 1A (AVPR1A): implications for autism. *Mol Autism* 2011;**2**:3.
26. Meyer-Lindenberg A, Domes G, Kirsch P, Heinrichs M. Oxytocin and vasopressin in the human brain: social neuropeptides for translational medicine. *Nat Rev Neurosci* 2011;**12**:524−38.
27. Bielsky IF, Hu S-B, Szegda KL, Westphal H, Young LJ. Profound impairment in social recognition and reduction in anxiety-like behavior in vasopressin V1a receptor knockout mice. *Neuropsychopharmacol* 2003;**29**:483−93.
28. Sakakibara M, Felix-Ortiz AC, Febo M. Gestational valproate alters BOLD activation in response to complex social and primary sensory stimuli. *PLoS One* 2012;**7**:e37313.
29. Umbricht D, del Valle Rubido M, Hollander E, McCracken JT, Shic F, Scahill L, et al. A single dose, randomized, controlled proof-of-mechanism study of a novel vasopressin 1a receptor antagonist (RG7713) in high-functioning adults with autism spectrum disorder. *Neuropsychopharmacol* 2016;**42**:1914−23.
30. Weiss A, Wilson VAD, Hopkins WD. Early social rearing, the V1A arginine vasopressin receptor genotype, and autistic traits in chimpanzees. *Autism Res* 2021;**14**:1843−53.
31. Kimi S, Maiti R, Srinivasan A, Mishra BR, Hota D. Efficacy and safety of V1a receptor antagonists in autism spectrum disorder: a meta-analysis. *Int J Dev Neurosci* 2023;**84**:3−13.
32. László K, Vörös D, Correia P, Fazekas CL, Török B, Plangár I, et al. Vasopressin as possible treatment option in autism spectrum disorder. *Biomedicines* 2023;**11**:2603.
33. Glavaš M, Gitlin-Domagalska A, Dębowski D, Ptaszyńska N, Łęgowska A, Rolka K. Vasopressin and its analogues: from natural hormones to multitasking peptides. *Int J Mol Sci* 2022;**23**:3068.
34. Baska F, Bozó É, Patócs T. Vasopressin receptor antagonists: a patent summary (2018−2022). *Expert Opin Ther Pat* 2023;**33**:385−95.

35. Yamamura Y, Ogawa H, Chihara T, Kondo K, Onogawa T, Nakamura S, et al. OPC-21268, an orally effective, nonpeptide vasopressin V1 receptor antagonist. *Science* 1991;**252**:572−4.

36. Serradeil-Le Gal C, Wagnon J, Garcia C, Lacour C, Guiraudou P, Christophe B, et al. Biochemical and pharmacological properties of SR 49059, a new, potent, nonpeptide antagonist of rat and human vasopressin V1a receptors. *J Clin Investig* 1993;**92**:224−31.

37. Fabio KM, Guillon CD, Lu S-F, Heindel ND, Brownstein MJ, Lacey CJ, et al. Pharmacokinetics and metabolism of SRX246: a potent and selective vasopressin 1a antagonist. *J Pharm Sci* 2013;**102**:2033−43.

38. Brownstein MJ, Simon NG, Long JD, Yankey J, Maibach HT, Cudkowicz M, et al. Safety and tolerability of SRX246, a vasopressin 1a antagonist, in irritable huntington's disease patients—a randomized phase 2 clinical trial. *J Clin Med* 2020;**9**:3682.

39. Lago TR, Brownstein MJ, Page E, Beydler E, Manbeck A, Beale A, et al. The novel vasopressin receptor (V1aR) antagonist SRX246 reduces anxiety in an experimental model in humans: a randomized proof-of-concept study. *Psychopharmacology* 2021;**238**:2393−403.

40. Maibach HT, Brownstein MJ, Hersch SM, Anderson KE, Itzkowitz DE, Damiano EM, et al. The vasopressin 1a receptor antagonist SRX246 reduces aggressive behavior in Huntington's disease. *J Pers Med* 2022;**12**:1561.

41. Ratni H, Rogers-Evans M, Bissantz C, Grundschober C, Moreau JL, Schuler F, et al. Discovery of highly selective brain-penetrant vasopressin 1a antagonists for the potential treatment of autism *via* a chemogenomic and scaffold hopping approach. *J Med Chem* 2015;**58**:2275−89.

42. Schnider P, Bissantz C, Bruns A, Dolente C, Goetschi E, Jakob-Roetne R, et al. Discovery of balovaptan, a vasopressin 1a receptor antagonist for the treatment of autism spectrum disorder. *J Med Chem* 2020;**63**:1511−25.

43. Bolognani F, del Valle Rubido M, Squassante L, Wandel C, Derks M, Murtagh L, et al. A phase 2 clinical trial of a vasopressin V1a receptor antagonist shows improved adaptive behaviors in men with autism spectrum disorder. *Sci Transl Med* 2019;**11**:eaat7838.

44. Hollander E, Jacob S, Jou R, McNamara N, Sikich L, Tobe R, et al. Balovaptan *vs* placebo for social communication in childhood autism spectrum disorder. *JAMA Psychiatry* 2022;**79**:760−9.

45. Jacob S, Veenstra-VanderWeele J, Murphy D, McCracken J, Smith J, Sanders K, et al. Efficacy and safety of balovaptan for socialisation and communication difficulties in autistic adults in North America and Europe: a phase 3, randomised, placebo-controlled trial. *Lancet Psychiat* 2022;**9**:199−210.

46. Fabio K, Guillon C, Lacey CJ, Lu SF, Heindel ND, Ferris CF, et al. Synthesis and evaluation of potent and selective human V1a receptor antagonists as potential ligands for PET or SPECT imaging. *Bioorg Med Chem* 2012;**20**:1337−45.

47. Naik R, Valentine H, Hall A, Mathews WB, Harris JC, Carter CS, et al. Development of a radioligand for imaging V1a vasopressin receptors with PET. *Eur J Med Chem* 2017;**139**:644−56.

48. Haider A, Xiao Z, Xia X, Chen J, Van RS, Kuang S, et al. Development of a triazolobenzodiazepine-based PET probe for subtype-selective vasopressin 1A receptor imaging. *Pharmacol Res* 2021;**173**:105886.

49. Rong J, Haider A, Jeppesen TE, Josephson L, Liang SH. Radio-chemistry for positron emission tomography. *Nat Commun* 2023;**14**:3257.

50. Abbott NJ. Prediction of blood−brain barrier permeation in drug discovery from *in vivo, in vitro* and *in silico* models. *Drug Discov Today Technol* 2004;**1**:407−16.

51. Kunwittaya S, Nantasenamat C, Treeratanapiboon L, Srisarin A, Isarankura-Na-Ayudhya C, Prachayasittikul V. Influence of logBB cut-off on the prediction of blood−brain barrier permeability. *Biomed Appl Technol J* 2013;**1**:16−34.

52. Wager TT, Hou X, Verhoest PR, Villalobos A. Moving beyond rules: the development of a central nervous system multiparameter optimization (CNS MPO) approach to enable alignment of druglike properties. *ACS Chem Neurosci* 2010;**1**:435−49.

53. Łabuzek K, Suchy D, Gabryel B, Bielecka A, Liber S, Okopień B. Quantification of metformin by the HPLC method in brain regions, cerebrospinal fluid and plasma of rats treated with lipopolysaccharide. *Pharmacol Rep* 2010;**62**:956−65.

54. Deng X, Rong J, Wang L, Vasdev N, Zhang L, Josephson L, et al. Chemistry for positron emission tomography: recent advances in ^{11}C-, ^{18}F-, ^{13}N-, and ^{15}O-labeling reactions. *Angew Chem Int Ed* 2019;**58**:2580−605.

55. Pettibone DJ, Kishel MT, Woyden CJ, Clineschmidt BV, Bock MG, Freidinger RM, et al. Radioligand binding studies reveal marked species differences in the vasopressin V_1 receptor of rat, rhesus and human tissues. *Life Sci* 1992;**50**:1953−8.

56. Gal CSL, Raufaste D, Marty E, Garcia C, Maffrand JP, Le Fur G. Autoradiographic localization of vasopressin V_{1a} receptors in the rat kidney using [^{3}H]-SR 49059. *Kidney Int* 1996;**50**:499−505.

57. Vågnes ØB, Hansen FH, Christiansen REF, Gjerstad C, Iversen BM. Age-dependent regulation of vasopressin V_{1a} receptors in pre-glomerular vessels from the spontaneously hypertensive rat. *Am J Physiol-renal* 2004;**286**:F997−1003.

58. Smith CJW, Poehlmann ML, Li S, Ratnaseelan AM, Bredewold R, Veenema AH. Age and sex differences in oxytocin and vasopressin V1a receptor binding densities in the rat brain: focus on the social decision-making network. *Brain Struct Funct* 2016;**222**:981−1006.

59. Grazzini E, Breton C, Derick S, Andres M, Raufaste D, Rickwaert F, et al. Vasopressin receptors in human adrenal medulla and pheochromocytoma1. *J Clin Endocr Metab* 1999;**84**:2195−203.

60. Uchida Y, Ohtsuki S, Katsukura Y, Ikeda C, Suzuki T, Kamiie J, et al. Quantitative targeted absolute proteomics of human blood−brain barrier transporters and receptors. *J Neurochem* 2011;**117**:333−45.

61. Tan Z, Haider A, Zhang S, Chen J, Wei J, Liao K, et al. Quantitative assessment of translocator protein (TSPO) in the non-human primate brain and clinical translation of [^{18}F]LW223 as a TSPO-targeted PET radioligand. *Pharmacol Res* 2023;**189**:106681.

62. Ottoy J, Verhaeghe J, Niemantsverdriet E, Wyffels L, Somers C, De Roeck E, et al. Validation of the semiquantitative static suvr method for ^{18}F-AV45 PET by pharmacokinetic modeling with an arterial input function. *J Nucl Med* 2017;**58**:1483−9.

63. Yan X, Siméon FG, Liow J-S, Morse CL, Montero Santamaria JA, Jenkins M, et al. *In vivo* evaluation of a novel ^{18}F-labeled PET radioligand for translocator protein 18 kDa (TSPO) in monkey brain. *Eur J Nucl Med Mol Imaging* 2023;**50**:2962−70.

64. Maher BS, Vladimirov VI, Latendresse SJ, Thiselton DL, McNamee R, Kang M, et al. The AVPR1A gene and substance use disorders: association, replication, and functional evidence. *Biol Psychiatry* 2011;**70**:519−27.

65. Nishina K, Takagishi H, Takahashi H, Sakagami M, Inoue-Murayama M. Association of polymorphism of arginine-vasopressin receptor 1a (*AVPR1a*) gene with trust and reciprocity. *Front Hum Neurosci* 2019;**13**:230.

66. Tanaka H, Nishina K, Shou Q, Takahashi H, Sakagami M, Matsuda T, et al. Association between arginine vasopressin receptor 1A (*AVPR1A*) polymorphism and inequity aversion. *Proc Biol Sci* 2023;**290**:20230378.

67. Yung-Chi C, Prusoff WH. Relationship between the inhibition constant (K_I) and the concentration of inhibitor which causes 50 per cent inhibition (I_{50}) of an enzymatic reaction. *Biochem Pharmacol* 1973;**22**:3099−108.

68. Gartzke D, Fricker G. Establishment of optimized MDCK cell lines for reliable efflux transport studies. *J Pharm Sci* 2014;**103**:1298−304.

69. Tournier N, Cisternino S, Peyronneau MA, Goutal S, Dolle F, Scherrmann JM, et al. Discrepancies in the P-glycoprotein-mediated

transport of ^{18}F-MPPF: a pharmacokinetic study in mice and non-human primates. *Pharm Res* 2012;**29**:2468−76.

70. Su L, Dalby KS, Luehmann H, Elkassih SA, Cho S, He X, et al. Ultrasmall, elementary and highly translational nanoparticle X-ray contrast media from amphiphilic iodinated statistical copolymers. *Acta Pharm Sin B* 2023;**13**:1660−70.

71. McLaren DG, Kosmatka KJ, Oakes TR, Kroenke CD, Kohama SG, Matochik JA, et al. A population-average MRI-based atlas collection of the *Rhesus macaque*. *Neuroimage* 2009;**45**:52−9.

72. Akaike H. A new look at the statistical model identification. *IEEE Trans Automat Control* 1974;**19**:716−23.